

Catalytic Au Wool-Ball-Shaped Nanostructures

Xiuxiu Yin,^[a] Nagappa L. Teradal,^[a] Ahiud Morag,^[a, b] and Raz Jelinek*^[a, b]

Gold nanoparticles shaped like wool balls were synthesized through the simple, spontaneous crystallization/reduction of gold thiocyanate $[\text{Au}(\text{SCN})_4^-]$ in water, without co-addition of nucleating seeds, templating compounds, or reducing agents. The Au nanowool balls were highly uniform in size and displayed a remarkable nanoribbon surface morphology. Size and

structural modulation of the particles were accomplished through the tuning of the concentration of the gold complex, as well as upon adding small quantities of organic solvents. The unique corrugated morphology and high surface area of the Au nanowool balls enabled their use as effective catalytic substrates for methanol oxidation and nitrophenol reduction.

Introduction

Gold nanostructures, particularly Au nanoparticles (NPs) have attracted significant scientific and technological interest due to their physical properties and applications in electronics, optics, catalysis, biology, and sensing.^[1] The sizes, shapes, and surface features of Au NPs constitute the fundamental parameters affecting their properties and applications. Accordingly, broad research efforts have focused on the development of synthetic routes aimed at tailoring Au NP structure and surface properties.^[2] While most Au NPs reported thus far exhibit spherical shapes and smooth surface architectures, gold particles exhibiting rough or corrugated surfaces have been sought for important applications such as sensing and catalysis, which benefit from extended surface areas. Varied wrinkled/branched Au NP morphologies have been reported, including polyhedral NPs,^[3] dendritic nanostructures,^[4] star-shaped,^[5] flowery NPs,^[6,7] urchin-like,^[8] and others. The challenges, however, for fabricating irregularly shaped and non-smooth Au NPs in a controlled and practical manner are significant. Most reported strategies are relatively complex, consisting of multistep processes, and requiring the addition of reducing agents, seeds, and/or templates.^[9] Furthermore, uniformity and structural reproducibility have been generally limited.

Au NPs have been employed as catalytic substrates in varied reactions, including aerobic oxidation of alcohols,^[10] carbon monoxide oxidation,^[11] degradation of nitro-aromatic compounds,^[12] and others. Importantly, the catalytic efficiency of Au NPs has been linked to their sizes, shapes, and surface properties.^[11b,13] In particular, wrinkled/branched Au NP mor-

phologies are of interest for catalysis applications, as such particles exhibit high specific surface areas and abundant edges and crevices presumed to contribute to catalytic activity. Porosity is another important determinant for the catalytic activity of Au NPs; recent studies have demonstrated, for example, 50% enhancement of electrocatalytic activity attained in nanoporous Au NPs compared to porous gold sheets.^[14] Au “nanoflowers”, which combine nanoporosity and wrinkled surface morphology, have similarly displayed good catalytic properties for the degradation of nitroaromatic compounds.^[12b] Herein, we describe the generation of unique Au “nanowool balls” and their application as broad-based catalytic substrates. The Au nanowool balls were prepared through a simple process comprising self-assembly and reduction of $\text{Au}(\text{SCN})_4^-$ in water without co-addition of nucleation seeds, templates, or reducing agents. The nanowool-balls were highly uniform in size and shape, which could be tuned by modulating the reaction conditions. We demonstrate that the Au nanowool balls exhibited excellent catalytic activity for methanol oxidation and 4-nitrophenol degradation, ascribed to the intricate surface nanoribbon morphology.

Results and Discussion

Figure 1 depicts the synthetic scheme of the Au nanowool balls, and analytical characterization of the particles. The spontaneous self-assembly process is outlined in Figure 1A. Following dissolution of $\text{KAu}(\text{SCN})_4$ in the aqueous solution, Au nanoparticles exhibiting intertwined sheet morphology gradually grew, forming spherical particles mimicking wool-balls within a few hours. The scanning electron microscopy (SEM) images in Figure 1B highlight the particle growth process and morphology. Small Au nanoparticles exhibiting sizes of 30 ± 3 nm appeared within 2 h after dissolving $\text{KAu}(\text{SCN})_4$ in water (Figure 1B, left image). NPs exhibiting diameters of around 300 nm were observed after 8 h, adopting interweaved nanosheet structures (Figure 1B, middle image). The Au nanowool balls reached maximal growth 16 h after dissolution of the gold complex in water, and the rightmost SEM image in Figure 1B

[a] X. Yin, Dr. N. L. Teradal, A. Morag, Prof. R. Jelinek
Ben-Gurion University of the Negev
Department of Chemistry
Beer Sheva 84105 (Israel)
E-mail: razj@bgu.ac.il

[b] A. Morag, Prof. R. Jelinek
Ilse Katz Institute for Nanotechnology
Ben-Gurion University of the Negev
Beer Sheva 84105 (Israel)

Supporting information for this article can be found under:
<https://doi.org/10.1002/cctc.201700459>.

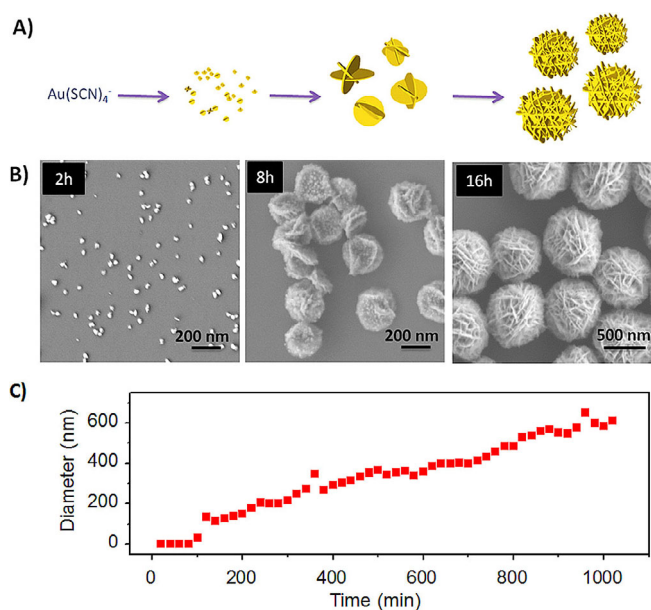


Figure 1. Synthesis of the Au nanowool balls and analysis of the growth process. A) Scheme depicting the Au nanowool ball assembly. B) SEM images depicting Au NPs formed 2, 8, and 16 h after dissolution of the $\text{Au}(\text{SCN})_4^-$ in water. C) Kinetics of particle diameter growth determined by dynamic light scattering (DLS). The time indicated corresponds to measurement after dissolution of the $\text{Au}(\text{SCN})_4^-$ in water.

reveals abundant spherical particles exhibiting diameters of 650 ± 50 nm, displaying remarkable nanoribbon morphology. Transmission electron microscopy (TEM) data presented in Figure S1A,B indicate that while the inner cores of the Au nanowool balls are not hollow, the corrugated nanoribbon morphology is extended deep within the Au nanoparticle. The Au nanowool balls were fairly uniform in size (see inset in Figure S1C for the size distribution analysis).

Figure 1C depicts a kinetic analysis of the nanowool-ball growth carried out by using dynamic light scattering (DLS). The DLS experiment in Figure 1C complements the SEM study (Figure 1B) and highlights the gradual particle growth. Notably, similar to the leftmost SEM image in Figure 1B, distinguishable particles appeared only after approximately 1.5 h, consistent with the initial assembly of nucleation seeds in the aqueous solution, which subsequently enlarged into nanowool balls. Figure 1C also points to a particle diameter plateau of around 650 nm, consistent with the SEM data in Figure 1B. The polydispersity index of the DLS analysis presented in Figure S2 yielded values of 0.035–0.158, confirming a relatively narrow particle size distribution.

To elucidate the structural features and assembly mechanism of the Au nanowool balls we carried out X-ray photoelectron spectroscopy (XPS) and X-ray diffraction (XRD) analyses (Figure 2). The XPS spectrum of the particles features superimposed peaks of Au^0 at 84.2 eV and 87.9 eV, and low-area signals at 85.4 eV and 88.8 eV corresponding to Au^I ions (approximately 15% abundance as compared to the Au^0 peaks),^[15] confirming that the nanowool-ball structures comprise of predominantly metallic gold and additional Au^I (Figure 2A i). Previous studies have reported that Au^I ions constitute intermediate

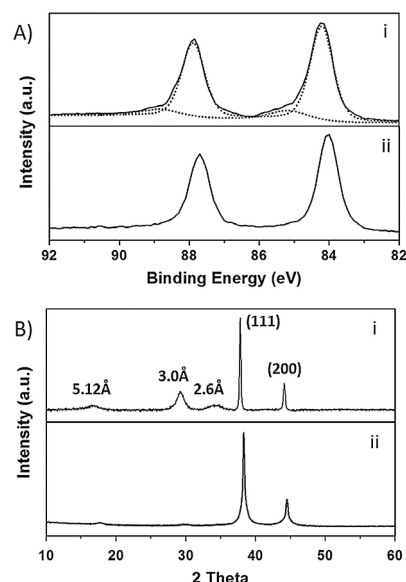


Figure 2. Spectroscopic characterization of the Au nanowool balls. A) X-ray photoelectron spectra (XPS) of the self-assembled Au colloids i) before and ii) after plasma treatment. The prominence of the Au^0 species is apparent. B) Powder XRD patterns of the gold nanoparticles i) before and ii) after plasma treatment.

species in the spontaneous reduction process of $\text{Au}(\text{SCN})_4^-$ in aqueous solutions.^[16] Plasma treatment of Au films is known to induce the efficient reduction of the metal.^[17] The electrons produced in the plasma chamber react with the residual Au^I ions, reducing them to crystalline gold. Indeed, treating the Au colloids with air plasma eliminated the Au^I XPS peaks to yield purely metallic gold particles (Figure 2A ii).

Powder XRD data presented in Figure 2B corroborates the XPS experiments, providing evidence for the crystalline nature of the Au nanowool balls. The powder XRD pattern of the as-synthesized colloids reveals two diffraction peaks at 38° and 45° corresponding to the $\text{Au}(111)$ and $\text{Au}(200)$ crystal planes, respectively (Figure 2B i). The low intensity XRD signals at 5.12 Å and 2.6 Å are attributed to partially organized crystalline structures of $\text{KAu}(\text{SCN})_2$.^[18] The presence of the Au^I thiocyanate complex is also supported by the XPS results in Figure 2A i. The Au^I ions are intermediate species in the reduction of the Au^{III} species in $\text{Au}(\text{SCN})_4^-$ induced by the thiocyanate ligands.^[16] An additional prominent peak at around 30° corresponds to a 3.0 Å inter-planar distance and is ascribed to crystalline assembly comprising $\text{KAu}(\text{SCN})_2$ units bonded through aurophilic interactions.^[19]

Aurophilic interactions between Au^I ions have been reported in varied gold assemblies, generating anisotropic metallic gold nanostructures.^[20] In the system presented in this study, the mechanism responsible for the wool-ball-like crystal growth is likely based upon aurophilic interactions between the Au^I ions in $\text{Au}(\text{SCN})_2^{1-}$ complexes. The linear configuration of aurophilic-bonded $\text{Au}(\text{SCN})_2^{1-}$ complexes facilitates planar crystalline growth, giving rise to the nanoribbon morphology. The anisotropic ribbon-like structures (Figure 1B), as well as the diffraction parameters in the XRD analysis (Figure 2B) both point to

the prominent role of aurophilic interactions in the assembly of the nanowool balls. Echoing the XPS analysis, virtually all the gold in the colloid sample was converted into Au⁰ after plasma treatment, as only the Au(111) and Au(200) crystal planes are observed (Figure 2 B ii).

We further investigated whether externally controlled experimental factors could modulate the structural features of the gold nanowool balls (Figure 3). Figure 3 A depicts the effect of

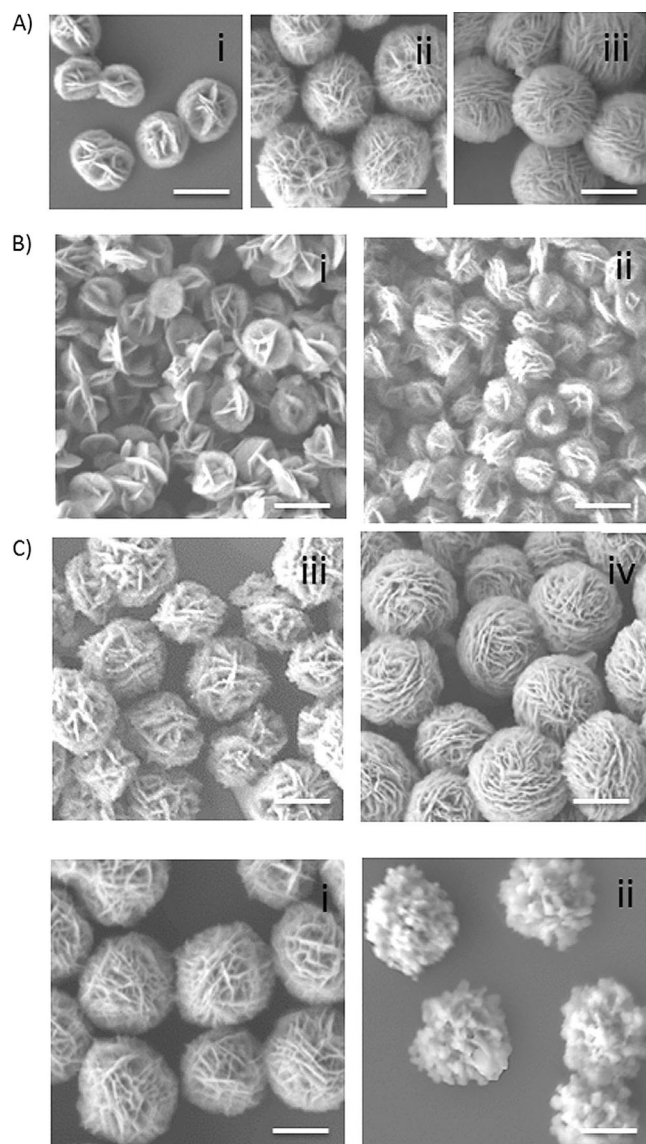


Figure 3. Effects of synthesis conditions upon Au nanowool-ball morphology. SEM images of the Au particles prepared under different experimental conditions. A) Different $\text{KAu}(\text{SCN})_4$ concentrations in the aqueous solution: i) 2 mM, ii) 5 mM, and iii) 10 mM. B) Organic solvents (10% v/v): i) acetone, ii) ethanol, and iii) DMF, iv) DMSO. C) Temperature effect: i) 25 °C and ii) 50 °C. Scale bars = 500 nm.

the concentration of $\text{KAu}(\text{SCN})_4$ upon the Au nanoparticles' morphology and size. Indeed, the SEM images in Figure 3 A demonstrate that higher concentrations of gold thiocyanate gave rise to larger colloid particles displaying a more dense

nanoribbon surface morphology. This outcome is consistent with the Au particle growth mechanism discussed above, as greater concentrations of the gold complex are expected to generate abundant and more condensed crystalline Au nanoribbons.

The effect of organic solvents co-added to the aqueous $\text{KAu}(\text{SCN})_4$ solution was also examined (Figure 3 B). The SEM images presented in Figure 3 B reveal that the addition of low concentrations of organic solvents (10% v/v) had noticeable effects upon the size and morphologies of the Au colloid particles. Acetone induced the most pronounced structural effect, giving rise to small gold particles (ca. 300 nm diameter, Figure 3 B i) comprising disk-like morphologies rather than curved nanoribbons. Addition of ethanol produced Au nanoparticles that were slightly bigger, although the particles' surface exhibited more abundant nanoribbons (Figure 3 B ii). The SEM image of Au particles grown in a dimethylformamide (DMF)/water solution (Figure 3 B iii) depicts larger Au colloid particles (diameters of ca. 500 nm) displaying relatively abundant intertwined nanoribbons.

Interestingly, co-addition of dimethylsulfoxide (DMSO) and $\text{Au}(\text{SCN})_4^-$ generated similarly sized nanoparticles, although their surface morphology featured very dense curved nanoribbons (Figure 3 B iv) that closely resemble the nanowool balls assembled in pure water (that is, Figure 1 B). The effects of the organic solvents upon assembly and structure of the Au colloid particles are ascribed to the intimate relationship between crystallization processes and solvent properties.^[21] In particular, we observe that the polarity of the solvent was correlated to the structural impact, as the polarity indexes of acetone and ethanol were close to each other (5.4 and 5.2, respectively), and considerably lower than DMF and DMSO (6.4 and 6.5, respectively).^[22] Elevated temperature had also a dramatic effect upon the Au nanoparticles (Figure 3 C). Specifically, increasing the temperature of the aqueous $\text{KAu}(\text{SCN})_4$ solution from 25 °C to 50 °C completely eliminated the intertwined nanoribbon morphology, instead generating particles comprising a roughly shaped surface morphology displaying irregularly shaped protruding domains (Figure 3 C ii). Similar particle morphologies were recorded in samples incubated at higher temperatures (Supporting Information, Figure S3).

Figures 4 and 5 demonstrate applications of the Au nanowool balls as effective substrates for electrocatalysis and heterogeneous catalysis. Figure 4 A presents the electrochemically active surface area analysis of the Au wool balls, carried out through electrochemical gold oxide stripping in 0.5 M H_2SO_4 at a scan rate of 5 mV s^{-1} . To determine the significance of the unique surface morphology of the Au nanowool balls, we also measured the electrochemically active surface areas of the Au NPs grown through incubation of $\text{KAu}(\text{SCN})_4$ at 50 °C—a temperature in which the particles formed did not exhibit the surface nanoribbon morphology (for example, SEM images in Figure 3 C ii). We also examined solid circa 100 nm-diameter Au NPs displaying smooth surface (SEM image in the Supporting Information, Figure S4).

Figure 4 A shows that the Au nanowool balls exhibit a lower oxidation peak, at 1.06 V, compared to both the Au particles

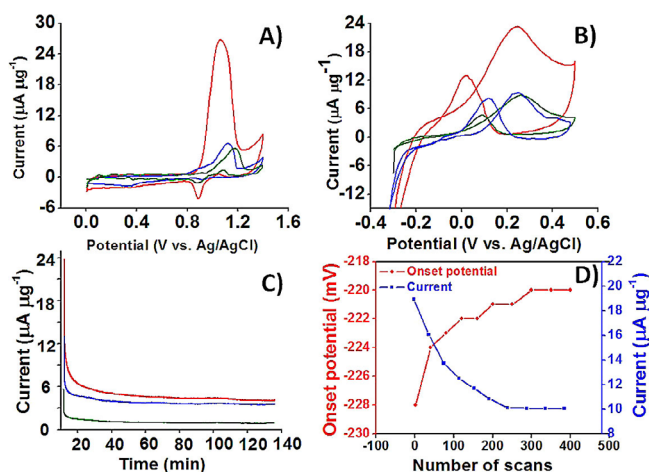


Figure 4. Electrochemical performance and methanol oxidation catalyzed by the Au nanowool balls. A) Oxide stripping curves of Au nanowool balls (red curve), Au wool balls prepared at 50 °C (blue), and conventional 100-nm Au nanoparticles (green), using modified electrodes in 0.5 M H₂SO₄ at a scan rate of 5 mV s⁻¹. Methanol oxidation catalysis measurements: B) Cyclic voltammograms and C) chronoamperograms utilizing the Au nanowool-balls (red), Au wool balls prepared at 50 °C (blue), and conventionally prepared 100-nm Au NPs (green) in deoxygenated solution of 0.5 M KOH and 2 M methanol. D) Stability and durability of the Au nanowool balls for methanol oxidation: Dependence of the onset potential (red line) and oxidation peak current (blue) upon number of scans.

synthesized at 50 °C (1.12 V) and conventional 100-nm Au NPs (1.18 V), indicating that surface atoms on the nanowool balls were more readily oxidized. The electrochemically active surface areas were quantified by integrating the areas under the gold oxide reduction curves near 0.9 V and assuming a specific charge of 450 $\mu\text{C cm}^{-2}$ for the gold oxide reduction. Electroactive surface areas of 10.34 $\text{m}^2 \text{g}^{-1}$, 1.10 $\text{m}^2 \text{g}^{-1}$, and 2.69 $\text{m}^2 \text{g}^{-1}$ were calculated for the Au nanowool balls, Au colloid particles prepared at 50 °C, and 100-nm Au NPs, respectively. These data clearly show that the nanowool balls exhibited substantial electroactive surface area available for catalysis (comparison of the electrochemical parameters obtained from Figure 4A is provided in the Supporting Information Table S1).

Figure 4B–D depicts application of the Au nanowool balls to methanol electro-oxidation catalysis. Figure 4B presents cyclic voltammetry (CV) curves, recorded in 2 M methanol and 0.5 M KOH solution, of Au nanowool balls (red curves), Au wool balls prepared at 50 °C (blue curves), and conventionally prepared 100-nm Au NPs (green curves). Figure 4B confirms that all NP samples exhibited the characteristic methanol electro-oxidation behavior.^[23] In case of the Au nanowool balls, an instantaneous surge in current was observed from -0.212 V(vs. Ag/AgCl) onwards in the positive potential scan mode. The current peaked at 0.24 V, reaching a maximum of 24 $\mu\text{A } \mu\text{g}^{-1}$ corresponding to the oxidation peak of methanol. In the negative sweeping scan mode, a second oxidation peak was recorded at 0.016 V in the reverse scan, attributed to the removal of the incompletely oxidized carbonaceous species formed in the forward scan. In comparison, Figure 4B indicates that both Au wool balls prepared at 50 °C and the 100-nm smooth NPs featured significantly reduced methanol oxidation peaks with cur-

rents of 11.5 $\mu\text{A } \mu\text{g}^{-1}$ and 8.8 $\mu\text{A } \mu\text{g}^{-1}$, respectively, at a relatively higher oxidation potential of 0.26 V for both NP species.

Furthermore, the Au nanowool balls exhibited a much lower onset potential (-0.212 V) than the high-temperature-prepared Au wool balls (-0.136 V) and smooth-surfaced 100-nm Au NPs (-0.087 V). Figure S5 in the Supporting Information compares the peak current determined according to the electroactive surface area and peak current calculated for Au mass. Notably, while the current-per-surface-area obtained for the Au nanowool balls was smaller than that for the Au particles prepared at 50 °C, the total electroactive surface area of the nanowool balls was significantly higher than the corresponding area of the Au colloid particles prepared at 50 °C. Overall, these results underscore excellent catalytic activity for methanol oxidation of the Au nanowool balls that is on par with or better than previous catalytic gold systems.^[14,24] Moreover, the significantly more pronounced catalytic performance of the Au nanowool balls compared to the two other Au NPs examined (Figure 4B) points to the crucial role of the corrugated surface morphology of the particles in promoting the catalytic activity.

Figure 4C examines the long-term electrocatalytic performance and tolerance of the Au nanowool balls in comparison with Au wool balls prepared at 50 °C and the 100-nm conventionally prepared Au NPs. The chronoamperometric curves in Figure 4C were recorded at 0.24 V (for the Au nanowool balls), 0.26 V (Au particles prepared at 50 °C), and 0.26 V (conventional Au NPs), corresponding to the respective oxidative peak potentials for the Au NP samples (Figure 4B). Figure 4C shows that the Au nanowool balls exhibited a gradual decrease in current, reaching a steady state at 6.2 $\mu\text{A } \mu\text{g}^{-1}$ after 60 min. In comparison, the currents of the Au particles prepared at 50 °C and conventional Au NPs decreased more significantly, diminishing to 2.7 $\mu\text{A } \mu\text{g}^{-1}$ and 0 $\mu\text{A } \mu\text{g}^{-1}$ after 60 min; the rapid current decrease reflects a greater accumulation of carbonaceous intermediates upon the surfaces of the Au NPs, which consequently deactivate catalytic sites.^[14] This performance is on par or better than previously reported gold-based methanol oxidation catalysts (Supporting Information, Table S2).

To adhere to the practical requirements of actual fuel cell applications, the stability of the nano Au wool-ball catalytic platform was evaluated by performing multiple electrocatalytic cycles of methanol oxidation (Figure 4D; the actual CV data are presented in Figure S6A). Figure 4D shows that the Au nanowool balls exhibited stable currents over 100 (ca. 12.5 $\mu\text{A } \mu\text{g}^{-1}$) and 400 cycles (ca. 10.1 $\mu\text{A } \mu\text{g}^{-1}$) with the retention of peak current of at least 70% and 50%, respectively.

We also calculated the tolerance ratios for methanol oxidation (I_f/I_b , in which I_f corresponds to forward oxidation peak current, and I_b corresponds to backward oxidation peak current), which reflect the extent of adsorption of “poisoning” intermediate carbonaceous species, which deactivate the catalysts’ surface (Supporting Information, Figure S6B).^[25] Specifically, a high tolerance ratio was determined for the Au nanowool balls ($I_f/I_b=2.6$) that was significantly higher than both the Au particles prepared at an elevated temperature ($I_f/I_b=1.6$) and conventional Au NPs ($I_f/I_b=1.1$). These results indicate

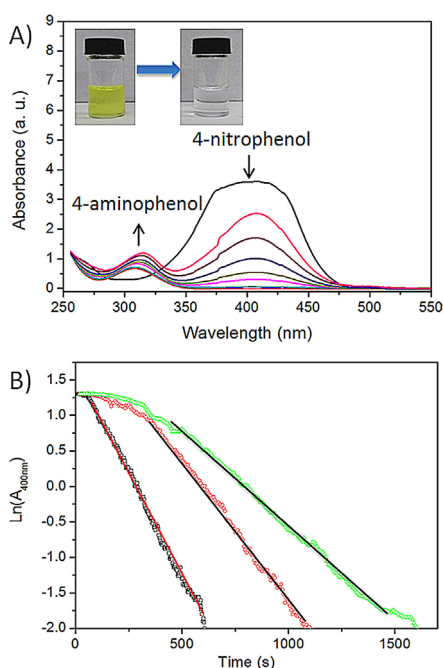


Figure 5. Au nanowool balls as catalysts for the degradation of 4-nitrophenol. A) Time-dependent UV/vis absorption spectra of aqueous solutions of 4-nitrophenol and NaBH_4 in the presence of the Au nanowool balls prepared at 25°C . B) Plots of the natural log of absorbance at 400 nm versus reaction time for the catalytic degradation of 4-nitrophenol by Au nanowool balls (black curve), Au NPs prepared at 50°C (red curve), and conventionally prepared 100-nm Au NPs (green curve).

the greater tolerance of the Au nanowool balls towards surface accumulation of carbonaceous species and further attest to the superior catalytic performance of these Au NPs.

Figure 5 depicts the catalytic activity of the Au nanowool balls towards reduction of 4-nitrophenol, demonstrating their broad-based catalytic properties. Reduction of 4-nitrophenol has been studied as a representative reaction catalyzed by Au nanoparticles.^[26] Figure 5A depicts time-dependent ultraviolet/visible (UV/vis) absorbance spectra of 4-nitrophenol added (together with NaBH_4) to a solution of Au nanowool balls that was prepared through incubation of gold thiocyanate at 25°C with a regular time interval of 1 min. The reaction progress was monitored by UV/vis spectroscopy at the characteristic peak of 4-nitrophenol (400 nm). The progressively suppressed intensities at 400 nm in Figure 5A indicate that 4-nitrophenol was reduced to 4-aminophenol, catalyzed by the Au NPs. Furthermore, the yellow color of the 4-nitrophenol solution gradually faded upon progression of the reaction (Figure 5A). Importantly, no 4-nitrophenol reduction was observed without the Au nanowool balls, attesting to the crucial catalytic role of the Au particles in the reaction.

Figure 5B compares the catalytic activity of the Au nanowool balls, Au colloids prepared at 50°C with 100-nm Au NPs. With excess NaBH_4 and sufficient catalyst, the catalytic reduction of 4-nitrophenol is pseudo-first-order and dependent only on the concentration of 4-nitrophenol. We studied the correlation between the natural log of absorbance at 400 nm and reaction time. Linearity is observed for all reactions on these catalysts. The slopes of the lines reflect the apparent rate constant

(k_{app}) of the reaction for these three catalysts under the same reaction conditions. Importantly, the calculated k_{app} values were $5.92 \times 10^{-3} \text{ s}^{-1}$ (nanowool balls), $4.04 \times 10^{-3} \text{ s}^{-1}$ (Au wool balls prepared at 50°C) and $2.64 \times 10^{-3} \text{ s}^{-1}$ (conventional Au NPs). Indeed, the most pronounced k_{app} recorded for the reaction catalyzed by the Au nanowool balls attests to the greater catalytic capabilities of these unique gold nanoparticles.

Conclusions

We report production of unique Au nanowool balls through a simple synthetic route comprising dissolution of $\text{KAu}(\text{SCN})_4$ in water, without co-addition of nucleating seeds, reducing agents, or templating agents. The generated nanowool balls exhibited a narrow size distribution that could be tuned by external parameters such as the complex concentration or co-addition of organic solvents. The Au nanowool balls adopted a striking interwoven nanoribbon surface morphology that was dependent upon the solution temperature and low concentrations of organic solvents. The Au particles exhibited excellent broad-based catalytic properties, both for methanol oxidation as well as 4-nitrophenol reduction. The corrugated, high surface area morphology was likely the key factor contributing to the catalytic performance of the Au nanowool balls; indeed, the surface morphology also gave rise to interesting SERS properties (Supporting Information, Figure S7). Overall, this study expands the universe of Au nanoparticle morphologies, demonstrating the fabrication of catalytically active size-tunable Au nanoparticles in water through an extremely simple assembly process employing a readily available gold complex.

Experimental Section

Materials: $\text{HAuCl}_4 \cdot 3\text{H}_2\text{O}$, KSCN, NaBH_4 , 4-nitrophenol and *p*-aminothiophenol (PATP) were purchased from Sigma–Aldrich. Methanol, acetone, ethanol, dimethylformamide, dimethyl sulfoxide and H_2SO_4 were purchased from Bio Lab (Israel). The above-listed reagents were used as received. Water used in the experiments was doubly purified by a Barnstead D7382 water purification system (Barnstead Thermolyne, Dubuque, IA), at a resistivity of $18.3 \text{ M}\Omega \text{ cm}$.

Synthesis of the $\text{KAu}(\text{SCN})_4$ complex: 1 mL of an aqueous solution of $\text{HAuCl}_4 \cdot 3\text{H}_2\text{O}$ (24 mg mL^{-1}) was added to 1 mL of a solution of KSCN in water (60 mg mL^{-1}). The precipitate formed was separated by centrifugation at 4000 g for 10 min. The supernatant was decanted, and the residue was dried at room temperature.

Synthesis of Au nanowool balls: 5 mL of freshly prepared $\text{KAu}(\text{SCN})_4$ aqueous solution (5 mM) was placed in a glass vial. The solution was incubated at 25°C for 16 h, subsequently centrifuged at 1500 rpm for 5 min, and the precipitate was collected and washed with ultrapure deionized water three times and re-dispersed in acetone.

Synthesis of solid 100-nm gold nanoparticles. 100-nm gold nanoparticles were prepared according to a published procedure.^[27] A volume of 50 mL of HAuCl_4 ($10^{-2}\%$ by weight) is heated to boiling and 0.21 mL of trisodium citrate (1% by weight) is added. Reduction of gold chloride is practically complete after boiling for 5 min.

Electrochemical measurements: Electrochemical measurements of various samples were performed in 0.5 M KOH and 0.5 M H₂SO₄ solution using the standard three-electrode configuration. The working electrode used was gold-nanostructure- (Au wool balls, control, and solid 100-nm Au NPs) modified glassy carbon electrode (GCE), a saturated Ag/AgCl electrode as reference, and the counter electrode was a Pt wire. The as-prepared gold nanostructure dispersion was loaded onto a glassy carbon electrode (3 mm in diameter) by drop casting 2 μ L of the gold nanostructure dispersion. The methanol oxidation activity evaluated by cyclic voltammetric and chronoamperometric techniques.

Electrochemical active surface area: The electrochemical active surface area (EASA) of the gold nanostructure was explored using cyclic voltammetric techniques. The surface redox behavior of the gold nanostructures were characterized in 0.5 M H₂SO₄ at a scan rate of 5 mV s⁻¹. EASA was evaluated by using the equation $Q_0 = 2eN_A\Gamma_0A$, where Q_0 is the charge passed during the reduction of gold oxide, calculated by the integration of the gold oxide reduction peak, N_A is Avogadro constant, and Γ_0 is the surface concentration of atomic oxygen and A is the electroactive surface area. The specific charge equivalent of 450 μ C cm⁻² was used for converting the charge passed during the gold oxide reduction to a total surface area ($A = Q_0/450$), which was then divided by the mass of the Au nanowool ball to obtain a specific surface area per unit mass.

Catalytic reduction of 4-nitrophenol: A sodium borohydride solution (1.5 mL, 0.3 M) was added to a 4-nitrophenol solution (2 mL, 0.65 mM) within an optical cell. 0.5 mL of sample containing 30 mg L⁻¹ of Au NPs was added to the NaBH₄/4-nitrophenol solution (nanowool balls were previously treated for 5 min with air plasma, PDC-32G, Harrick plasma). The catalytic performance of the samples was monitored using a JASCO V-550 UV/vis spectrophotometer.

Dynamic light scattering (DLS) measurements: DLS data was collected at 25 °C on an ALV-CGS-8F instrument (ALV-GmbH, Germany) at 90deg (unless otherwise indicated), and the CONTIN method was used to obtain hydrodynamic radii (Rh). Prior to measurement, solutions were filtered through 0.45 and/or 0.22 μ m polyvinylidene fluoride (PVDF) Millipore filters.

Instruments and characterization: Scanning electron microscopy (SEM) was conducted with a JEOL (Tokyo, Japan) model JSM-7400F scanning electron microscope equipped with EDS (Thermo Scientific). Powder X-ray diffraction (XRD) measurements were carried out on a Panalytical Empyrean powder diffractometer equipped with a parabolic mirror on the incident beam providing quasi-monochromatic Cu_{K α} radiation ($\lambda = 1.54059$ Å) and an X'Celerator linear detector. X-ray photoelectron spectroscopy (XPS) analysis was conducted using a Thermo Fisher ESCALAB 250 instrument with a basic pressure of 2×10^{-9} mbar. The samples were irradiated in two different areas using monochromatic Al_{K α} 1486.6 eV X-rays, using a beam size of 500 μ m.

Acknowledgements

This work was supported by the Israel Science Foundation grant 201/14.

Conflict of interest

The Authors declare no conflict of interest.

Keywords: catalytic gold nanostructures · gold complexes · gold nanoparticles · methanol oxidation · porosity

- [1] a) Z. Quan, Y. Wang, J. Fang, *Acc. Chem. Res.* **2013**, *46*, 191–202; b) M.-C. Daniel, D. Astruc, *Chem. Rev.* **2004**, *104*, 293–346; c) C. Burda, X. Chen, R. Narayanan, M. A. El-Sayed, *Chem. Rev.* **2005**, *105*, 1025–1102; d) S. Eustis, M. A. El-Sayed, *Chem. Soc. Rev.* **2006**, *35*, 209–217; e) M. Zhu, B. Lei, F. Ren, P. Chen, Y. Shen, B. Guan, Y. Du, T. Li, M. Liu, *Sci. Rep.* **2014**, *4*, 5259; f) I. Akita, Y. Ishida, T. Yonezawa, *Bull. Chem. Soc. Jpn.* **2016**, *89*, 1054–1056; g) N. S. Abadeer, C. J. Murphy, *J. Phys. Chem. C* **2016**, *120*, 4691–4716; h) G. Yue, S. Su, N. Li, M. Shuai, X. Lai, D. Astruc, P. Zhao, *Coord. Chem. Rev.* **2016**, *311*, 75–84.
- [2] a) G. Maiorano, L. Rizzello, M. A. Malvindi, S. S. Shankar, L. Martiradonna, A. Falqui, R. Cingolani, P. P. Pompa, *Nanoscale* **2011**, *3*, 2227–2232; b) L. Xu, W. Ma, L. Wang, C. Xu, H. Kuang, N. A. Kotov, *Chem. Soc. Rev.* **2013**, *42*, 3114–3126.
- [3] a) Y. Ma, J. Zeng, W. Li, M. McKiernan, Z. Xie, Y. Xia, *Adv. Mater.* **2010**, *22*, 1930–1934; b) J. E. Millstone, S. J. Hurst, G. S. Métraux, J. I. Cutler, C. A. Mirkin, *Small* **2009**, *5*, 646–664; c) S. S. Shankar, A. Rai, A. Ahmad, M. Sastry, *Chem. Mater.* **2005**, *17*, 566–572.
- [4] S. Yi, L. Sun, S. C. Lenaghan, Y. Wang, X. Chong, Z. Zhang, M. Zhang, *RSC Adv.* **2013**, *3*, 10139–10144.
- [5] a) C. L. Nehl, H. Liao, J. H. Hafner, *Nano Lett.* **2006**, *6*, 683–688; b) L. Rodríguez-Lorenzo, R. A. Alvarez-Puebla, F. J. G. de Abajo, L. M. Liz-Marzán, *J. Phys. Chem. C* **2010**, *114*, 7336–7340.
- [6] a) J. Xie, Q. Zhang, J. Y. Lee, D. I. Wang, *ACS nano* **2008**, *2*, 2473–2480; b) C. Song, N. Zhou, B. Yang, Y. Yang, L. Wang, *Nanoscale* **2015**, *7*, 17004–17011.
- [7] C. Y. Song, B. Y. Yang, W. Q. Chen, Y. X. Dou, Y. J. Yang, N. Zhou, L. H. Wang, *J. Mater. Chem. B* **2016**, *4*, 7112–7118.
- [8] a) J. Li, J. Wu, X. Zhang, Y. Liu, D. Zhou, H. Sun, H. Zhang, B. Yang, *J. Phys. Chem. C* **2011**, *115*, 3630–3637; b) J. Li, J. Zhou, T. Jiang, B. Wang, M. Gu, L. Petti, P. Mormile, *Phys. Chem. Chem. Phys.* **2014**, *16*, 25601–25608.
- [9] a) J. E. Millstone, G. S. Métraux, C. A. Mirkin, *Adv. Funct. Mater.* **2006**, *16*, 1209–1214; b) C. Li, K. L. Shuford, Q. Park, W. Cai, Y. Li, E. J. Lee, S. O. Cho, *Angew. Chem.* **2007**, *119*, 3328–3332; c) Z. Li, W. Li, P. H. Camargo, Y. Xia, *Angew. Chem. Int. Ed.* **2008**, *47*, 9653–9656; *Angew. Chem.* **2008**, *120*, 9799–9802.
- [10] a) H. Tsunoyama, H. Sakurai, Y. Negishi, T. Tsukuda, *J. Am. Chem. Soc.* **2005**, *127*, 9374–9375; b) H. Liu, Y. Liu, Y. Li, Z. Tang, H. Jiang, *J. Phys. Chem. C* **2010**, *114*, 13362–13369; c) H. Tsunoyama, N. Ichikuni, H. Sakurai, T. Tsukuda, *J. Am. Chem. Soc.* **2009**, *131*, 7086–7093.
- [11] a) V. Zielasek, B. Jürgens, C. Schulz, J. Biener, M. M. Biener, A. V. Hamza, M. Bäumer, *Angew. Chem. Int. Ed.* **2006**, *45*, 8241–8244; *Angew. Chem.* **2006**, *118*, 8421–8425; b) M. Ojeda, B.-Z. Zhan, E. Iglesia, *J. Catal.* **2012**, *285*, 92–102.
- [12] a) H. Zhu, X. Ke, X. Yang, S. Sarina, H. Liu, *Angew. Chem.* **2010**, *122*, 9851–9855; b) K. Mao, Y. Chen, Z. Wu, X. Zhou, A. Shen, J. Hu, *J. Agric. Food Chem.* **2014**, *62*, 10638–10645.
- [13] a) A. T. Bell, *Science* **2003**, *299*, 1688–1691; b) H. Abe, J. Liu, K. Ariga, *Mater. Today* **2016**, *19*, 12–18; c) M. Shao, Q. Chang, J.-P. Dodelet, R. Chenitz, *Chem. Rev.* **2016**, *116*, 3594–3657; d) E. Yamamoto, K. Kuroda, *Bull. Chem. Soc. Jpn.* **2016**, *89*, 501–539.
- [14] S. Pedireddy, H. K. Lee, W. W. Tjui, I. Y. Phang, H. R. Tan, S. Q. Chua, C. Troadec, X. Y. Ling, *Nat. Commun.* **2014**, *5*, 4947.
- [15] Z. Huo, C.-k. Tsung, W. Huang, X. Zhang, P. Yang, *Nano Lett.* **2008**, *8*, 2041–2044.
- [16] A. Morag, N. Froumin, D. Mogiliansky, V. Ezersky, E. Beilis, S. Richter, R. Jelinek, *Adv. Funct. Mater.* **2013**, *23*, 5663–5668.
- [17] S. W. Lee, D. Liang, X. Gao, R. M. Sankaran, *Adv. Funct. Mater.* **2011**, *21*, 2155–2161.
- [18] J. Akola, M. Walter, R. L. Whetten, H. Häkkinen, H. Grönbeck, *J. Am. Chem. Soc.* **2008**, *130*, 3756–3757.
- [19] N. L. Coker, J. A. Krause Bauer, R. Elder, *J. Am. Chem. Soc.* **2004**, *126*, 12–13.
- [20] a) H. Ecken, M. M. Olmstead, B. C. Noll, S. Attar, B. Schlyer, A. L. Balch, *J. Chem. Soc. Dalton Trans.* **1998**, 3715–3720; b) H. Schmidbaur, A. Schier, *Chem. Soc. Rev.* **2008**, *37*, 1931–1951.

- [21] a) J. Zeng, Y. Ma, U. Jeong, Y. Xia, *J. Mater. Chem.* **2010**, *20*, 2290–2301; b) V. Amendola, S. Polizzi, M. Meneghetti, *J. Phys. Chem. B* **2006**, *110*, 7232–7237; c) W. J. Peveler, I. P. Parkin, *RSC Adv.* **2013**, *3*, 21919–21927.
- [22] R. E. Schirmer, *Modern methods of pharmaceutical analysis, Vol. 2*, CRC press, Boca Raton, **1990**, pp. 305–305.
- [23] H. Xu, L.-X. Ding, C.-L. Liang, Y.-X. Tong, G.-R. Li, *NPG Asia Mater.* **2013**, *5*, e69.
- [24] a) H. Li, Y.-J. Li, L.-L. Sun, X.-L. Zhao, *Electrochim. Acta* **2013**, *108*, 74–78; b) J.-J. Feng, Z.-Y. Lv, S.-F. Qin, A.-Q. Li, Y. Fei, A.-J. Wang, *Electrochim. Acta* **2013**, *102*, 312–318; c) C. Yu, F. Jia, Z. Ai, L. Zhang, *Chem. Mater.* **2007**, *19*, 6065–6067.
- [25] a) Z. Liu, X. Y. Ling, X. Su, J. Y. Lee, *J. Phys. Chem. B* **2004**, *108*, 8234–8240; b) R. Mancharan, J. B. Goodenough, *J. Mater. Chem.* **1992**, *2*, 875–887.
- [26] a) L. Shi, Q. Yu, Y. Mao, H. Huang, H. Huang, Z. Ye, X. Peng, *J. Mater. Chem.* **2012**, *22*, 21117–21124; b) M. Mohan, N. Mohan, D. K. Chand, *J. Mater. Chem. A* **2015**, *3*, 21167–21177; c) Y.-C. Chang, D.-H. Chen, *J. Hazard. Mater.* **2009**, *165*, 664–669; d) K. B. Narayanan, N. Sakthivel, *J. Hazard. Mater.* **2011**, *189*, 519–525.
- [27] G. Frens, *Nature Phys. Sci.* **1973**, *241*, 20–22.

Manuscript received: March 15, 2017

Revised manuscript received: March 20, 2017

Accepted manuscript online: May 9, 2017

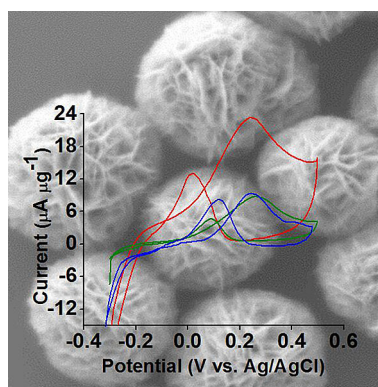
Version of record online: ■ ■ ■ ■, 0000

FULL PAPERS

X. Yin, N. L. Teradal, A. Morag, R. Jelinek*



Catalytic Au Wool-Ball-Shaped Nanostructures



Catalytic Au nanowool balls: Gold nanoparticles with a wool-ball surface morphology exhibit remarkable structural and catalytic properties. Size and structural modulation of the particles were accomplished through the tuning of the concentration of the gold complex and addition of small amounts of organic solvents. The Au nanowool balls were used as effective catalysts for methanol oxidation and nitrophenol reduction.